Solar Phys (2010) 265: 159–186
DOI 10.1007/s11207-010-9588-2

Reconstructing CME Structures from IPS Observations Using a Phenomenological Model

S.J. Tappin · T.A. Howard

Received: 25 March 2010 / Accepted: 3 June 2010 / Published online: 6 July 2010

Abstract We present an extension of the Tappin – Howard (TH) phenomenological model (Tappin and Howard, *Space Sci. Rev.* **147**, 55, 2009) for coronal mass ejection reconstruction to use interplanetary scintillation g-map data. The necessary changes to the model are discussed. We then use the modified model to reconstruct two major interplanetary disturbances observed using the Cambridge 3.6 ha Array in September 1980. We find that despite the lower cadence of IPS observations compared with white-light imagers, a consistent reconstruction can be generated which is in agreement with *in-situ* measurements and solar observations.

Keywords Coronal mass ejections · Interplanetary

1. Introduction

Coronal mass ejections (CMEs) are important phenomena for the evolution of the solar cycle as they are the mechanisms by which the Sun explosively releases large quantities of plasma and magnetic energy from the corona (Low, 1996). They may be described as large clouds of plasma within an erupting magnetic field, contain masses of the order of 10^{13} kg and have been observed to achieve speeds greater than 3000 $\mathrm{km\,s^{-1}}$ (see the CDAW Catalogue of LASCO CMEs http://cdaw.gsfc.nasa.gov/CME_list/index.html). A CME contains more energy than all of the other solar eruptive phenomena combined including solar flares, erupting prominences and solar energetic particles (Emslie *et al.*, 2004).

Remote Sensing of the Inner Heliosphere
Guest Editors: M.M. Bisi and A.R. Breen

S.J. Tappin (✉)
National Solar Observatory, Sacramento Peak, Sunspot, NM, USA
e-mail: jtappin@nso.edu

T.A. Howard
Southwest Research Institute, Boulder, CO, USA
e-mail: howard@boulder.swri.edu

Along with their importance towards our scientific understanding of solar cycle evolution, CMEs are also important to the technological community, as when they impact the Earth they are known to significantly increase geomagnetic activity (see, *e.g.*, Dungey, 1963), causing the most severe space weather effects known as (geo)magnetic storms. Magnetic storms are responsible for a variety of damaging effects to spacecraft, aircraft and technological infrastructure including spacecraft damage and destruction, power station failure and increased radiation dosage to aircraft passengers and astronauts. Consequently the study of CMEs has become an area of great interest to the scientific and technological communities (see, *e.g.*, Baker *et al.*, 2009).

CMEs are traditionally observed with white-light coronagraphs that block out the bright light from the solar disk revealing the faint surrounding corona. Because of their faintness relative to the corona, the most successful coronagraphs for CME detection have been on board spacecraft, from the early days of OSO-7 (Tousey, 1973) and Skylab (Gosling *et al.*, 1974) to the more recent LASCO (Brueckner *et al.*, 1995) and the STEREO/CORs (Howard *et al.*, 2008). Statistical studies of CMEs using coronagraphs include St. Cyr, Hundhausen, and Burkepile (1992), Hundhausen, Burkepile, and St. Cyr (1994), and St. Cyr *et al.* (2000).

Tracking CMEs beyond the range of coronagraphs is both more problematic and has a longer history than tracking them with coronagraphs. Interplanetary shocks were measured by the first suitably-equipped spacecraft to leave the Earth's magnetosphere (Sonett *et al.*, 1964; Gosling *et al.*, 1968). Since that time the interplanetary manifestations of CMEs and their associated shocks have been tracked by many *in-situ* platforms. These interplanetary counterparts of CMEs are often called ICMEs, but here we find it more convenient to use CME for all stages of the evolution of the disturbance. For space weather purposes the most significant *in-situ* platforms have been ISEE-3 (*International Sun-Earth Explorer-3*, 1978 – 1982, Ogilvie, von Rosenvinge, and Durney, 1977) and ACE (*Advanced Composition Explorer*, 1997-present, Stone *et al.*, 1998) both of which operated in orbit about the L1 point. A detector at the L1 point is about 1.5×10^6 km upstream of Earth and so detects Earth-directed interplanetary disturbances on the order of one hour before they reach Earth.

In more recent times the white-light imagers SMEI (Eyles *et al.*, 2003) and the HIs on STEREO (Eyles *et al.*, 2009) have been able to track CMEs as they propagate from the Sun. The geometrical challenges of interpreting these data have been discussed in a series of three papers by the authors (Howard and Tappin, 2009a, 2009b; Tappin and Howard, 2009). However white-light imaging is not the only technique capable of imaging and tracking CMEs through the heliosphere; by the late 1970's interplanetary scintillation observations had developed to a state where they could truly image CMEs. In this paper we revisit some of the observations of that era and re-interpret them using the techniques that we have developed for white-light images.

2. The IPS Dataset

Since the interplanetary scintillation (IPS) dataset used here is about 30 years old and has not been discussed much in the recent literature, it is worth our while to describe it in some detail, along with the physical processes involved.

IPS was first discovered in the early 1960's (Hewish, Scott, and Wills, 1964). It is the flickering of radio sources with small angular size ($\lesssim 1''$ in diameter) caused by density fluctuations (ΔN_e) along the line of sight between the source and the observer. These density fluctuations create a random phase-changing screen through which the radio waves must propagate. Since on a scale smaller than the typical size of an irregularity, the density gradients appear as a local prism. It can thus be seen that parts of the wavefront will be deflected

by a small angle and will then interfere with waves that have passed through different parts of the medium. Since this is a random process the interference will be constructive in some places and destructive in others. Provided that the angular size of the source is small compared with that of the irregularities, the net result of this is a random variation of intensity as we scan across the wavefront. Since the solar wind propagates outwards from the Sun, the motion of the medium transverse to the line of sight causes this pattern to move past the observer, resulting in a flickering of the source. For a detailed discussion of the physics and mathematics of scattering by irregular media, see the series of three papers by Budden and Uscinski (1970, 1971, 1972), and the papers by Tatarskii (1993) and Shishov (1993).

The level of scintillation is measured by the scintillation index (m)

$$m \equiv \frac{\Delta S_{\mathrm{RMS}}}{S}, \tag{1}$$

where S is the flux of the radio source and ΔS_{RMS} is the RMS fluctuation of the measured flux over the observing interval. In practice, as we show below, it is necessary only to measure ΔS which is advantageous as S is much more difficult to determine owing to confusion (Scheuer, 1957) and to the fact that many radio sources have a compact scintillating component embedded in a more diffuse non-scintillating component. Provided that the phase variations are small compared with one radian, the level of scintillation gives a measure of the integral of ΔN_{e} along the line of sight (Readhead, Kemp, and Hewish, 1978).

Houminer and Hewish (Houminer, 1971; Houminer and Hewish, 1972) showed that variations in scintillation levels could be correlated with structures in the solar wind. It was further shown by Tappin (1986) that the integrated turbulence is a good proxy for the integrated density along the line of sight, with a relationship that $N_{\mathrm{e}} \propto \Delta N_{\mathrm{e}}^{0.5}$ for transient disturbances (CMEs). It should here be noted that since the model used in this study fits only leading edges, the precise relationship between ΔN_{e} and N_{e} is not particularly important, only that they are strongly correlated.

The data used in this study come from observations made using the 3.6 Hectare Array near Cambridge between February 1980 and March 1981. This was a phased array operating at an observing frequency of 81.5 MHz (3.68 m wavelength) observing 16 beams in declination at meridian transit. Since the E – W size of the antenna was 128λ this means that each source was observed for about two minutes every 24 hours. The scintillating fluxes were determined using hardware scintillometers, thus reducing the required data rate to a level that allowed all 16 beams to be processed by the hardware available at that time, at the cost of losing the ability to do power-spectral analyses of the scintillation. The location of the antenna at about 52°N means that observations were limited to the area of sky north of declination 7°S.

Within that area, it was possible to identify 2246 sources suitable for space weather measurements (note that this is rather more than the number of sources listed in the IPS catalogue (Purvis *et al.*, 1987) which was generated from the same dataset, because for these purposes it does not matter if a deflection is due to a single source or the superposition of multiple sources). This grid is shown in Right Ascension and Declination (of date) coordinates in Figure 1. For each source a scintillation – elongation ($m(\varepsilon)$) curve was fitted. The ratio between each daily observation and the $m(\varepsilon)$ curve for the source was then calculated to give the enhancement factor (g):

$$g \equiv \frac{m_{\mathrm{observed}}}{m_{\mathrm{fitted}}} = \frac{\Delta S_{\mathrm{observed}}}{\Delta S_{\mathrm{fitted}}} \tag{2}$$

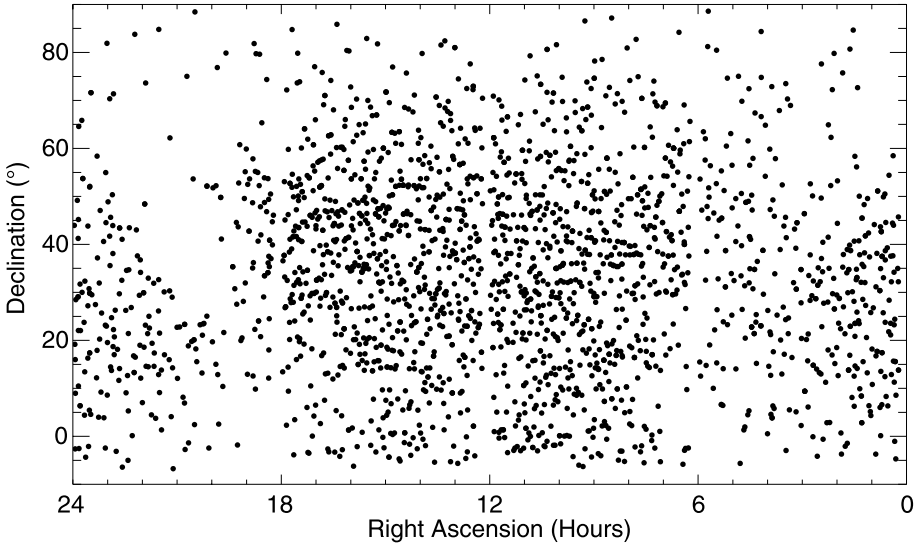

Figure 1 The grid of sources used to generate the IPS heliospheric images. The gaps at right ascensions of 0, 6, 12 and 18 hours correspond to the telescope noise-level calibrations. The band of thinner coverage running approximately from (24 h RA, 80° Dec) to (18 h, 0°) and from (6 h, 0°) to (0 h, 80°) is the region of the galactic plane.

(Gapper *et al.*, 1982). By using ratios it was possible to eliminate the fact that sources have widely different fluxes (and that the absolute flux may be poorly determined), and also to a very great extent the differences due to different source sizes.

The values of g can then be displayed in a number of ways to produce a heliospheric image. Historically, the Mollweide projection in heliocentric ecliptic coordinates was used (see, *e.g.*, Tappin, 1987), however in recent times the Hammer – Aitoff projection has been more widely used by instruments such as SMEI (see, *e.g.*, Tappin *et al.*, 2004) and for that reason we use the latter projection in this paper.

Two formats for the data are commonly used.

i) A symbol plot in which each radio source is represented by a symbol, red for enhanced scintillation and blue for reduced, and the more lines a symbol contains the larger the deviation of g from 1. Historically this was the primary data format, although to our knowledge it has not previously been shown in any publications.

ii) A greyscale (or colour) plot where the data are binned and the values of $\log_{10} g$ are averaged in each bin. Here we use 4° bins, compared with the 10° bins used in earlier analyses (Tappin, 1984, 1987).

These two formats are illustrated in Figure 2, along with the key to the symbol plots. We have generally found that the greyscale plots are easier for quickly spotting a disturbance, but that edges can be more-accurately determined from the symbol plots.

3. The TH Model and Its Modification for IPS

The Tappin – Howard (TH) model for optical white-light imagers has been described, and its effectiveness demonstrated by Tappin and Howard (2009) and Howard and Tappin (2010),

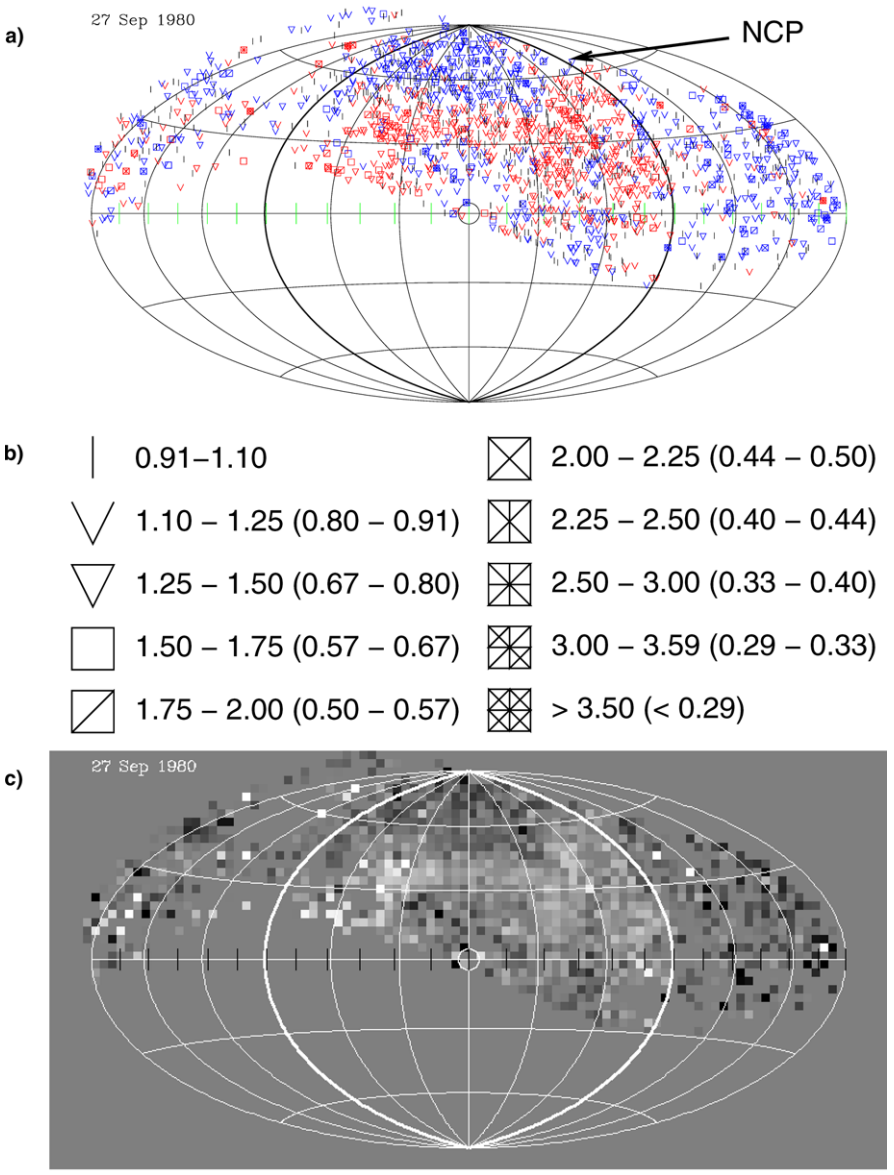

Figure 2 Map formats used in this paper. (a) The symbol plot format. (b) A key to the symbols in the symbol format, the first range is for the red symbols and the second (parenthesised) range is for blue. (c) The greyscale plot format. Each image is accumulated over a 24-hour interval, with lines of equal time joining the celestial poles which for all the images in this paper lie near 66N90W (marked as NCP in (a)) and 66S90E. The tick marks on the ecliptic plane indicate hours of the day running from right to left. It will be noted that a number of sources lie outside the grid to the East (left), this artifice is adopted to allow each map to be built from one day of data, and also to prevent discontinuities of time within the map.

along with a review of the underlying geometry and physics (Howard and Tappin, 2009a). So here we give a brief outline of the principles of the model and then concentrate on how this has been modified to work for IPS.

The TH model is a phenomenological model based on leading-edge measurements of CMEs observed at large distances from the Sun. The model takes advantage of the breakdown of linearity when CMEs are observed across large distances, so it is only applicable to CME observations across large regions of the sky.

A demonstration of its utility as a space weather forecasting tool has also been reported by Howard and Tappin (2010). This publication shows that for a small sample of events the speed of operation and accuracy of reconstruction are impressive, with arrival-time predictions, for example, almost two orders of magnitude more accurate than existing CME forecasting models.

In summary, firstly a set of synthetic sky maps for a range of simple CME structures are computed, based on the spherical shells of Tappin (1987) or the cone model of Zhao, Plunkett, and Liu (2002) with the addition of a distortion parameter to describe "bubble-like" or "concave-out" events. The synthetic maps form a grid in heliocentric distance (height), central co-latitude, central longitude, latitude and longitude size and distortion parameter. To cover the ranges of parameters required needs in the region of four million synthetic sky maps (Howard and Tappin, 2010). The problem is simplified by reducing these to a database of leading-edge elongations as a function of position angle.

The observations are also reduced to a list of leading-edge elongations, position angles and times, and a list of regions of missing or bad data. A fitting procedure based on a genetic algorithm followed by a simplex fitting is used to deduce the starting height (at the start of the first image), speed, direction, size and shape for the CME based on these models by minimising the residual elongation errors between model and data. The use of a starting height rather than the time of launch is a computational convenience, the launch time can be determined from the speed, the starting height and the time of the first image. When sufficient observations are available, it is possible to do a second stage of fitting to estimate an acceleration or deceleration.

Since both IPS and Thomson scattering are evaluated as line-of-sight integrals of a scattering function (although in the case of Thomson scattering it is strictly a volume integral) the integration process as described by Howard and Tappin (2009a) and Tappin and Howard (2009) can be carried directly over. The Thomson scattering integrals however must be replaced by the IPS integral as described by Readhead, Kemp, and Hewish (1978), Kemp (1979), and Tappin (1987). From these we have

$$m^2 = \int_0^\infty f(r, \zeta, \eta) \frac{\beta(r)}{1+h^2} \frac{(4Z)^2}{(1+h^2)^2 + (4Z)^2} \, \mathrm{d}z, \tag{3}$$

where:

z $\equiv$ the distance from the Earth towards the source (note that this differs from the usage of Readhead, Kemp, and Hewish (1978) and Kemp (1979) who use distance from the point of closest approach to the Sun).

h $\equiv$ the source-size term, that is the reduction in scintillation index from the value for a point source: $h^2 = 2z^2\theta_0^2/a^2$. This term is important when the angular size of the source becomes comparable with the angular size of a typical irregularity.

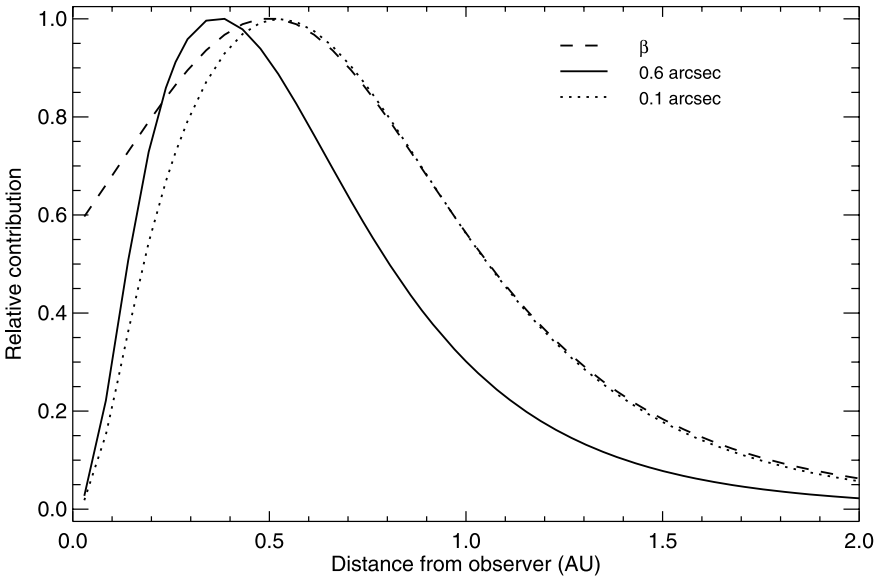

Figure 3 Comparison of the scattering weighting function for IPS with the raw phase variation. All the traces are computed at an observing frequency of 81.5 MHz for an elongation of 60°, and are normalised to a maximum of one.

Z ≡ the Fresnel filter, the reduction of scintillation contribution for plasma close to the observer, due to the apparent size of the irregularities being larger than the scattering angle: $Z = z/\kappa a^2 = z\lambda/2\pi a^2$.
$\beta(r)$ ≡ the scattering power $= \mathrm{d}\phi_0^2/\mathrm{d}z$.
$f(r, \zeta, \eta)$ ≡ the enhancement factor of turbulence at location (r, ζ, η) in the solar wind.
r, ζ, η ≡ heliocentric coordinates in the solar wind which can be determined from z and the direction of the line of sight.
a ≡ the scale size of the medium, which will be discussed below.
κ, λ ≡ the wavenumber and wavelength of the observing radio waves.
θ_0 ≡ the angular radius of the source.
r ≡ the radial distance from the Sun.

The values of the scattering power β and the scale size a are discussed in some detail by Readhead, Kemp, and Hewish (1978) and Kemp (1979) and we adopt their values. Namely:

$$a(r) = 175 r^{1/2}\,\mathrm{km} \quad \text{for } 0.2 < r < 0.6\ \mathrm{AU},$$
$$a(r) = 250 r^{5/4}\,\mathrm{km} \quad \text{for } r > 0.6\ \mathrm{AU},$$
$$\beta(r) = 2.73 \times 10^{-3} \lambda^2 r^{-4}\,\mathrm{rad}^2\,\mathrm{AU}^{-1} \quad \lambda \text{ in m}, r \text{ in AU}.$$

Since these expressions contain the observing wavelength and the source size it is necessary to select suitable values of these parameters for the computations. Naturally we have used the 3.6 ha Array observing frequency of 81.5 MHz or a wavelength of 3.68 m. Although the values of g do not depend strongly on the source size, we must nonetheless choose a typical value. We follow Tappin (1984, 1987) in using a source diameter of 0.6″ (*i.e.* $\theta_0 = 0.3''$).

At this point it is worthwhile to pause and consider the contributions of the main terms in Equation (3). In Figure 3 we display the phase variation (β and the integrand in Equation (3)

computed for a small (0.1″ diameter) source and a larger (0.6″ diameter) source. All are computed at an elongation of 60°, although the details will change at different elongations as is seen in Figure 8b of Howard and Tappin (2009a) (for Thomson scattering), the important features of the behaviour will be similar. When compared with the phase modulation, both scintillation index weights fall off rapidly close to the observer. This is due to the Fresnel filter term (Z in Equation (3)), and it represents the fact that close to the observer the angular deflections of the wavefront are small compared with the angular size of a typical irregularity in the medium (the scale size a), thus no interference occurs. For the small source, the scintillation contribution follows closely the phase modulation far from the observer, but for the larger source the contribution from the distant plasma is significantly reduced, this is the effect of the source-size term (h in Equation (3)), and can be seen as being significant at large distances due to the source size being larger than the angular projection of the scale size. This results in different parts of the source scintillating in different phases and thus reducing the levels of fluctuation.

Since at 81.5 MHz the effects of strong scattering become important near an elongation of 30°, and inside that the relation in Equation (3) breaks down, we do not compute the model inside 30°. It should also be noted that although it might be expected that increased scattering at small elongations would lead to values of g less than 1, Tappin (1984) was not able to detect this effect.

The models used were the "bent-shell" structures described by Howard and Tappin (2010), but with two significant differences:

i) We used the ratio of the scintillation index to the baseline level (*i.e.* the $g = m/m_0$ parameter, where m is from Equation (3) and m_0 is m computed with $f = 1$ everywhere) instead of a difference of brightness, and therefore the threshold levels to define an edge were also changed to use $g > 1.1$ as the primary level and $g > 1.07$ as the comparison, *c.f.* Tappin and Howard (2009). These levels were selected as it has been found that a 10% increase or decrease in g is about the smallest that can be reliably detected (Tappin, 1984).

ii) For the reasons discussed above, the computations were not continued inside an elongation of 30°.

The generation codes modified as above were used to produce a new database of leading edges which can then be used to fit the TH model to IPS data using the same fitting codes as for white-light images.

Since the IPS observations have a 24-hour cadence a CME is rarely if ever seen with a defined leading edge in more than four maps. It is therefore not feasible to run the Stage 2 fitting described by Tappin and Howard (2009) on groups of five images to determine accelerations. However, the main reason for running the Stage 2 fitting on groups of five orbits was to allow the CME to move sufficiently to get reliable speed measurements, however with the 24-hour cadence of IPS observations this is not an issue. Therefore in the analysis presented in this paper we have attempted to determine accelerations using pairs of maps.

4. Supporting Data

Although the inner heliosphere was well-observed during the maximum of Cycle 21, the data are not as readily available as for instruments operating in the "internet era", however a number of experiments have made their data available either from their own sites or via such repositories as the Virtual Heliospheric Observatory (VHO; http://vho.nasa.gov). Among those that we have examined are the following.

ISEE-3 & IMP8 (*Interplanetary Monitoring Platform*) Both of these provide near-Earth *in-situ* magnetic field and plasma measurements. A merged one-hour dataset is available in hard-copy form (Couzens and King, 1986), while higher-resolution data for the individual instruments can be found on the UC Berkeley STEREO/IMPACT site (http://sprg.ssl.berkeley.edu).

Pioneer Venus Orbiter PVO was in orbit around Venus and carried (*inter alia*) a magnetometer and plasma detector. Hourly data for both are on VHO, and high-resolution magnetometer data can be obtained from the UCLA site of the Planetary Data System (http://www.igpp.ucla.edu).

Helios-1 Was in an elliptical orbit around the Sun, ranging from 0.3 to 1.0 AU. Data for both the plasma and magnetic field are on the VHO and the UC Berkeley STEREO/IMPACT site. *Helios-2* was not operating at this time.

SMM (*Solar Maximum Mission*) C/P Coronagraph data and CME lists are available via the High Altitude Observatory site (http://smm.hao.ucar.edu/smm/smmcp_cme.html). The authors have a copy of the HXIS dataset from their association with the University of Birmingham (UK).

SOLWIND Dr. N.R. Sheeley Jr. (Naval Research Laboratory) has provided a list of SOLWIND CMEs for September 1980, and also times when no images appear to be available.

Geomagnetic Indices Archives of geomagnetic indices are available from the SPIDR site (http://spidr.ngdc.noaa.gov), and from *Solar Geophysical Data* (1980, 1981).

Flares Listings of X-ray flares are available from NGDC (ftp://ftp.ngdc.noaa.gov/STP/SOLAR_DATA/SOLAR_FLARES/XRAY_FLARES). GOES X-ray plots are available in *Solar Geophysical Data* (1980, 1981).

5. The Events

One problem with attempting to apply the TH model to IPS observations is that because of the 24-hour cadence imposed by the rotation of the Earth, the majority of disturbances that reached Earth were seen for only one day prior to their arrival there. We have selected two events that were clearly seen with a leading edge for three or four days. These were a disturbance to the North-East first observed on 17 September 1980, and an apparently Earth-directed event first seen on 26 September 1980. Both of these have previously been analysed using "by eye" comparisons (Tappin, 1984, 1987).

5.1. 17 September 1980

The first event that we considered was seen to the NE from 17 September 1980. This event has already been described by Tappin (1987). Greyscale and symbol maps for this event are shown in the first two columns of Figure 4.

17 Sept. The disturbance was visible in the North-East just outside 30° as a very weak enhancement of scintillation. This is very close to the transition to strong scattering thus almost certainly suppressing the values of g. In the analysis of Tappin (1987) the presence of the feature on this day was not noticed (probably a consequence of working with paper maps).

18 Sept. This was the first day on which the feature was clearly visible. It appeared as a loop of enhanced scintillation to the NE reaching to near 90° at its greatest elongation.

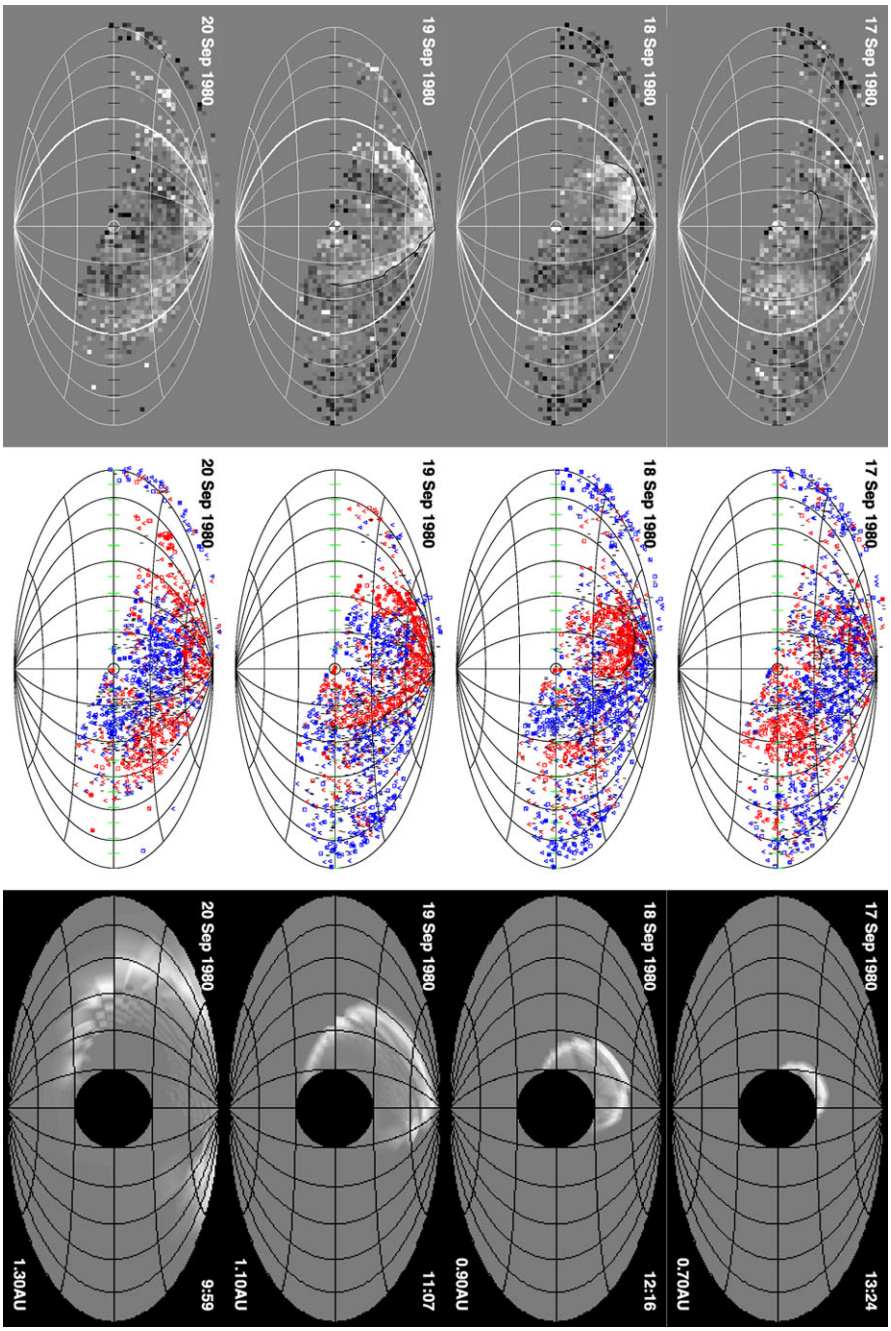

Figure 4 g-maps for the 17 September 1980 event. The left-hand column shows the greyscale format with a saturation range from $g = 0.5$ (black) to $g = 2.0$ (white). The centre column shows the symbol format. The right column shows the simulations from Run #3. The corresponding time is given in the top right of each simulation and the heliocentric distance of the CME centre is given bottom right as these are snapshots, while the observations span the whole day. Both are presented in the Hammer – Aitoff projection. The measured leading edge of the disturbance is also shown on both observation columns as a black curve.

Table 1 Summary of the fitting results for the TH model applied to the 17 September 1980 CME. Runs rejected as aberrant are indicated by struck-out rows, the run selected as "typical" is indicated in bold font. PCPA = projected central position angle, *i.e.* the position angle of the centre of the CME structure when projected into the sky. Error indicates the mismatch parameter as described by Tappin and Howard (2009) and is a measure of how well the computed leading edge agrees with the measurements.

Run#	Launch Date	Speed $km\,s^{-1}$	Lon.	Lat.	Lon. Size	Lat. Size	Dist-ortion	Error	PCPA
0	14/09/80 18:26	423.37	−23.29	36.01	32.71	36.01	1.25	6.48	34.76
1	13/09/80 09:09	297.67	−10.79	16.97	20.82	25.67	2.19	6.14	31.53
2	14/09/80 17:13	390.44	−17.05	24	27.38	37.03	1.34	6.02	33.37
3	**14/09/80 05:24**	**363.58**	**−17.96**	**22.68**	**24.03**	**38.5**	**1.65**	**5.78**	**36.43**
4	13/09/80 21:09	342.17	−17.11	22.28	24.47	48	1.76	6.38	35.68
5	13/09/80 19:35	328.36	−15.9	18	26.09	33.18	1.65	5.74	40.15
6	13/09/80 09:38	307.62	−17.12	17.83	30.29	19.56	1.52	6.15	42.47
7	14/09/80 06:32	366.22	−21.3	23.35	30	54.53	1.19	5.36	40.08
~~8~~	~~14/09/80 16:51~~	~~415.63~~	~~−35.11~~	~~29.09~~	~~48.27~~	~~49.07~~	~~0.62~~	~~5.98~~	~~45.96~~
9	14/09/80 06:02	366.1	−17.77	22.98	24.13	47.37	1.68	5.81	35.75
Avg	14/09/80 01:54	353.95	−17.59	22.68	26.66	37.76	1.58	5.99	36.69
Std	0.5	39.76	3.47	5.68	3.78	11.08	0.3	0.35	3.54
Med	14/09/80 05:24	363.58	−17.12	22.68	26.09	37.03	1.65	6.02	35.75
Min	13/09/80 09:09	297.67	−23.29	16.97	20.82	19.56	1.19	5.36	31.53
Max	14/09/80 18:26	423.37	−10.79	36.01	32.71	54.53	2.19	6.48	42.47

19 Sept. The loop had now clearly become larger and extended over most of the available position-angle range. Interpreting the differences in elongation between East and West requires proper allowance to be made for the near 10 hour time range between the observations of the flanks.

20 Sept. By this time, although enhanced scintillation was still visible, there was no longer a measurable leading edge. Decreased scintillation was clearly visible in the interior of the disturbance.

21 Sept. onwards These days are not shown in Figure 4, but the enhanced scintillation was entirely replaced by a decrease that persisted for a few days.

The TH model was applied to the measured leading edges with ten stage 1 runs that are summarised in Table 1. We have also calculated possible interaction times or closest approaches for Earth, *Pioneer Venus Orbiter* (PVO) and *Helios-1* although at this time PVO was 61°W of Earth at 0.72 AU, and *Helios-1* was 94.3°W and at 0.96 AU, so we would not expect this easterly disturbance to impact either (which is what the model found). These are summarised in Table 2.

It is immediately apparent from Table 1 that this disturbance was strongly curved with all the fits showing distortion parameters greater than one. For comparison the simple bubble such as was used by Tappin (1987) is approximated by a distortion parameter close to one.

As can be seen in Table 2, the vast majority of simulations predict that this disturbance will impact the Earth on 20 September. The spread in calculated impact times is relatively wide as the impact is near the flank of the disturbance and thus a small change in direction or curvature will cause a large change in the arrival time. Of the ten fits we ran, we have rejected No. 8 as clearly aberrant, since all of its parameters differ substantially from those of the

Table 2 Summary of the predicted interactions of the 17 September CME with *in-situ* observing spacecraft. The "Miss Distance" is the angle between the Earth and the nearest part of the CME as measured from the centre of the Sun, "Rcent" is the heliocentric distance of the centre of the CME when it hits the observer or at the time of the closest approach.

Run#	Earth				*Pioneer Venus Orbiter*				*Helios-1*			
	Hit?	Date	Miss Dist (°)	Rcent (AU)	Hit?	Date	Miss Dist (°)	Rcent (AU)	Hit?	Date	Miss Dist (°)	Rcent (AU)
0	0	20/09/80 08:24	2.52	1.36	0	18/09/80 18:53	50.51	0.98	0	19/09/80 21:41	79.2	1.26
1	1	20/09/80 03:37	0	1.16	0	18/09/80 12:49	49.7	0.89	0	20/09/80 06:03	81.51	1.18
2	1	20/09/80 05:22	0	1.24	0	18/09/80 20:45	47.71	0.94	0	20/09/80 05:56	78.04	1.25
3	**1**	**20/09/80 09:50**	**0**	**1.3**	**0**	**18/09/80 18:34**	**50.31**	**0.96**	**0**	**20/09/80 00:54**	**80.94**	**1.22**
4	1	20/09/80 10:52	0	1.3	0	18/09/80 23:44	48.31	1.01	0	20/09/80 16:35	79.05	1.35
5	1	20/09/80 01:05	0	1.18	0	18/09/80 16:20	49.48	0.92	0	20/09/80 07:14	81.1	1.23
6	0	19/09/80 18:15	2.89	1.13	0	17/09/80 23:31	57.07	0.81	0	19/09/80 12:08	88.71	1.08
7	1	20/09/80 04:33	0	1.25	0	18/09/80 21:50	47.75	0.98	0	20/09/80 10:55	78.18	1.31
~~8~~	~~1~~	~~20/09/80 05:35~~	~~0~~	~~1.33~~	~~0~~	~~18/09/80 22:20~~	~~48.21~~	~~1.02~~	~~0~~	~~20/09/80 08:10~~	~~76.57~~	~~1.35~~
9	1	20/09/80 10:42	0	1.31	0	18/09/80 22:57	48.87	0.99	0	20/09/80 06:19	79.44	1.27
Avg		20/09/80 05:24	0.6	1.25		18/09/80 17:16	49.97	0.94		20/09/80 04:25	80.69	1.24
Std		0.23	1.2	0.08		0.31	2.85	0.06		0.34	3.26	0.08
Med		20/09/80 05:22	0	1.25		18/09/80 18:53	49.48	0.96		20/09/80 06:03	79.44	1.25
Min		19/09/80 18:15	0	1.13		17/09/80 23:31	47.71	0.81		19/09/80 12:08	78.04	1.08
Max		20/09/80 10:52	2.89	1.36		18/09/80 23:44	57.07	1.01		20/09/80 16:35	88.71	1.35

other fits. Such aberrant solutions occasionally occur as a statistical anomaly of the fitting algorithm. We then selected No. 3 as a "typical" fit for further comparisons. We choose the fit "closest" to the median of all the fits rather than the lowest residual since we find that on occasion an outlying fit may have a low residual, but that on such occasions the errors surfaces are frequently found to be peculiar. At present the definition of closest is subjective, we hope to be able to define it more objectively when more events have been analysed with the TH Model (this work is currently in progress). The maps from Run 3 computed at the nearest 0.05 AU radial position to noon on each day are shown alongside the observations in Figure 4. This comparison shows the excellent agreement obtained between the model and observation.

To get an idea of how well constrained the parameters are, we compute error contours for selected pairs of parameters, some pairs are shown in Figure 5. The edges in the latitude and longitude parameters are a well-known artefact of the integration grid and are discussed by Tappin and Howard (2009). Other than this it is notable that the latitude and longitude sizes appear almost unconstrained; however, this is to be expected for a highly-curved structure where the edges are almost beyond the range of the observations (Figure 6).

The 3-D reconstruction shown in Figure 6 illustrates very clearly how close this disturbance came to missing the Earth.

The overall structure and direction that we compute is in acceptable agreement with the results obtained by eye in Tappin (1987) although we obtain a somewhat lower speed.

Since there are three measurements of the leading edge for this event it is possible to use the "stage 2" fitting to obtain two speeds. In the stage 2 fitting process the shape and direction are held constant while the speed and height are allowed to vary (Tappin and Howard, 2009). When this was done using Run No. 3 as the basis, we obtained the results shown in Figure 7. This shows a strong apparent deceleration. The speed inferred from 17 and 18 September of 476 $\mathrm{km\,s^{-1}}$ is comparable with the 500 $\mathrm{km\,s^{-1}}$ inferred in Tappin (1987), but the speed from 18 and 19 is much slower at 312 $\mathrm{km\,s^{-1}}$. We discuss the interpretation of this deceleration later.

During the time range of the possible launch of the event, neither SMM C/P data (Burkepile and St. Cyr, 1993) nor SOLWIND images (N.R. Sheeley Jr., private communication, 2009) were available. SMM/HXIS showed a small X-ray spike at about 19:00 UT on 13 September in AR2665 at 13N05E, but it was not sufficient to cause the instrument to enter its flare-mode. The GOES X-ray flare lists do not show any significant flares in the interval, although the western flank of the likely source lies on the extension of a line of minor N-hemisphere flares (Figure 8). The line of flares after the event that projects back to near the centre was in the southern hemisphere and thus unlikely to be connected. Based on this we think it probable that the CME was associated with the same region that produced the northern-hemisphere flares and the HXIS spike but that it was not associated with an identified flare.

Near-Earth plasma data were not available at the time of the earlier analysis by Tappin (1987). Now however, the merged IMP-8 & ISEE-3 dataset (Couzens and King, 1986) covers both CMEs considered in this paper, and higher-resolution magnetometer data from ISEE-3 are also available. These two datasets are shown in Figures 9 and 10. It is clear that within the time range covered by our fits a disturbance arrived at ISEE-3. This shows that the CME did indeed impact the Earth; however, since B_z was small or northward during the CME passage (having been southward prior to its arrival) it is not surprising that no significant geomagnetic disturbances were observed.

As is predicted by the fits, no significant features were seen at either PVO or *Helios-1* at this time.

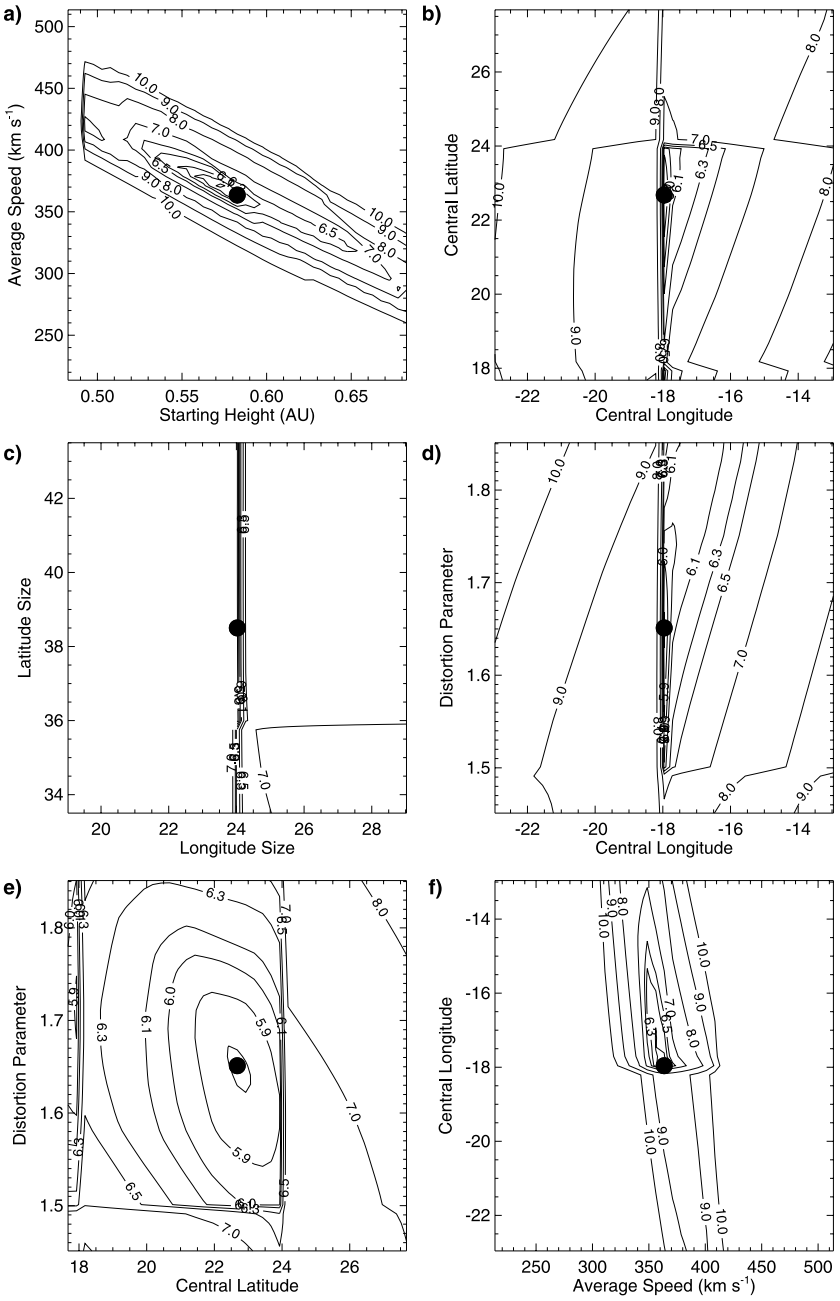

Figure 5 Error surfaces for selected pairs of fitting parameters for the 17 September 1980 disturbance. (a) height at 00:00 UT on 17 September *vs.* speed, (b) central latitude *vs.* central longitude, (c) latitude size (half-angle) *vs.* longitude size, (d) distortion parameter *vs.* central longitude, (e) distortion parameter *vs.* central latitude and (f) central longitude *vs.* speed. The values for each contour indicate the change in the mismatch parameter.

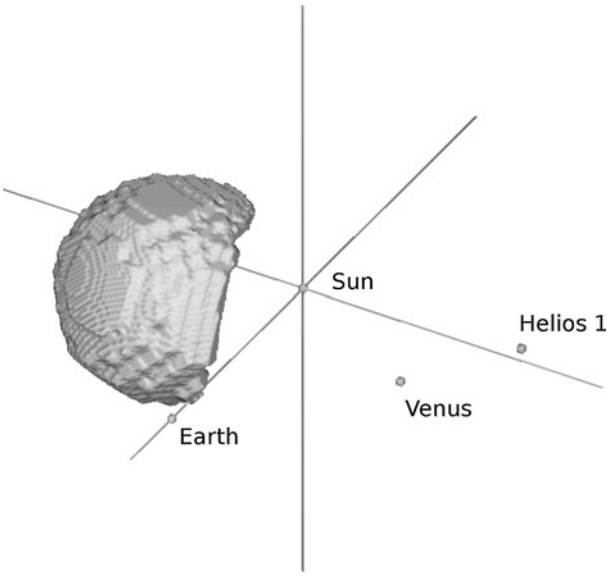

Figure 6 3-D view of the fitted leading surface for the 17 September 1980 disturbance, viewed from 35N30W, when the leading edge was at 1.2 AU (22:33 UT on 19 September). The locations of the Sun, Earth, Venus (PVO) and *Helios-1* are also shown.

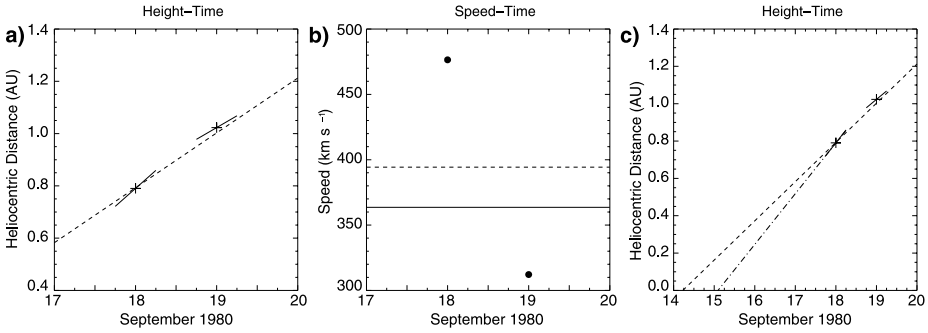

Figure 7 Stage 2 fitting results for the 17 September 1980 CME. (a) Detailed view of the height fits with the speeds indicated as the solid line through each point, (b) speed *vs.* time, the horizontal solid line is the speed from the Stage 1 fit, and the dashed line is the mean of the Stage 2 speeds. (c) Height *vs.* time, extrapolated back to the launch time (dashed line), also indicated is the extrapolation of the first speed back to the surface of the Sun (dash-dot line).

5.2. 26 September 1980

The second event considered was a very prominent "halo" (*i.e.* Earth-directed) disturbance seen from 26 September 1980. The maps for this event are shown in the first two columns of Figure 11. This event was presented as an example of a disturbance seen without significant confusion from other disturbances by Hewish (1993).

26 Sept. As with the previous event, the first day was overlooked in the original analysis (Tappin, 1984). The disturbance was seen as a weak enhancement to the North-East just outside 30° elongation. In the West, it was impossible to see owing to the presence of an earlier event.

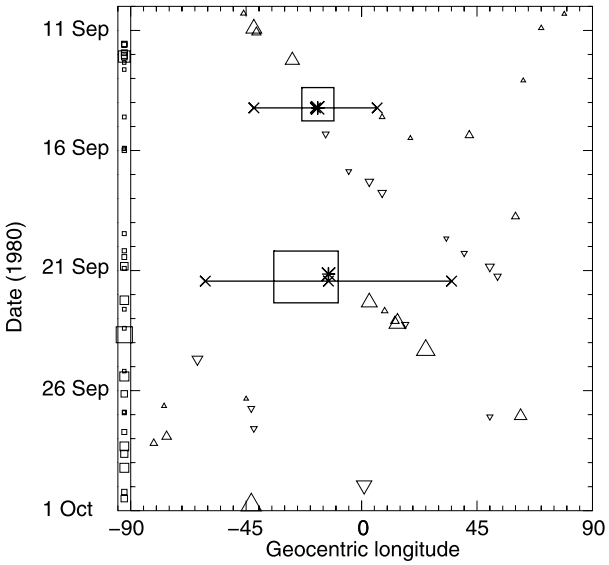

Figure 8 GOES X-ray flares above class C2 for the interval of the two events. The larger the symbol the brighter the flare, upward pointing triangles denote N-hemisphere, downward S-hemisphere and the squares in the left margin represent flares with no identified optical counterpart (which therefore cannot be located on the solar disk). For each IPS event a number of parameters derived from the stage 1 TH model fitting are added: the asterisk indicates the median launch date and longitude, the box the earliest and latest times and the extremal longitudes of the CME centre, the horizontal line shows the longitude range covered by the selected "typical" fit.

27 Sept. This is the first day when the feature was clearly visible. The region of enhanced scintillation extended over the whole range of position angle covered by the telescope. Part of the leading edge in the West could not be measured owing to the earlier disturbance (this region is the gap in the overplotted leading edge).

28 Sept. The disturbance now appeared as a very strong enhancement and was approaching 90° elongation in the East.

29 Sept. The leading edge could only be distinguished in the West. The scintillation levels were almost doubled in the strongest parts.

30 Sept. The whole observable sky beyond 90° now showed enhanced scintillation, and no leading edge could be seen. Nearer to the Sun scintillation levels had started to return to normal. As with the first event, decreased scintillation was seen over much of the sky for a few days following this event.

The TH model was applied to the measured leading edges with ten runs which are summarised in Table 3. As before we have also computed the arrival time at Earth and the times of closest approach to PVO and *Helios-1* (Table 4).

This event was clearly much nearer to the "classical" spherical shell than the other, and also exceptionally slow, well below the normal solar wind speed. We have again found it necessary to reject one fit, Run No. 0, as aberrant. All the fits hit the Earth, indeed given the halo-like appearance of the g-maps it would be very surprising if they did not. The arrival times for this event are much more tightly grouped with about three hours between the earliest and the latest, since this event was more spherical and Earth was nearer to the centre of the disturbance this is to be expected. Again we selected a "typical" fit for further analysis, in this case run No. 8. The simulated g-maps for this fit are compared with the observations in last column of Figure 11. Again we see a good agreement between the simulated maps and the observations when we allow for the time-smearing of the observations caused by the movement of the CME during the generation of the map, this is analogous to the distortion of fast-moving objects when photographed using a focal-plane shutter. The error surfaces (Figure 12) show that the speed and distortion are well constrained while the sizes are poorly constrained. In this case the reason is that the structure is large so that the edges are probably

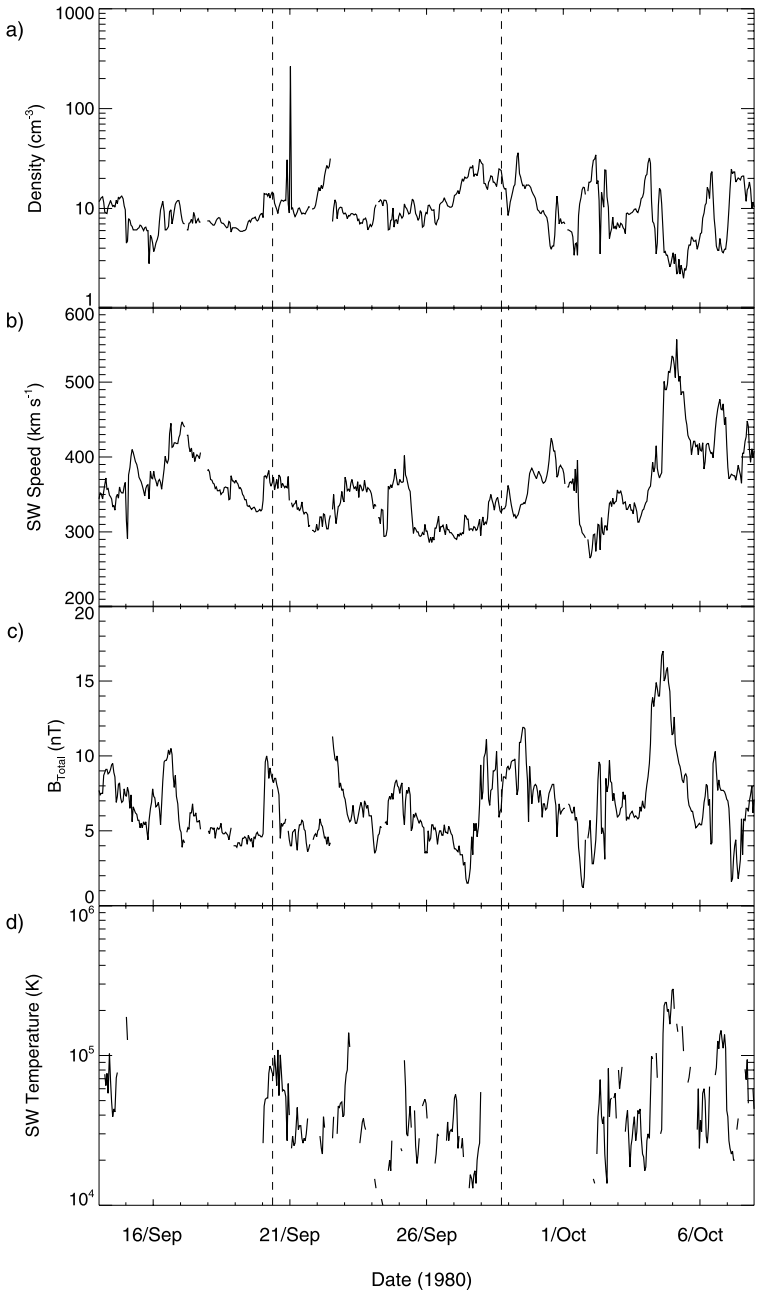

Figure 9 Overview of the near-Earth plasma and field data from the merged ISEE-3 & IMP-8 dataset: (a) density, (b) solar wind speed, (c) total magnetic field, and (d) solar wind proton temperature. The predicted times for the two events arriving at Earth are shown as vertical dashed lines.

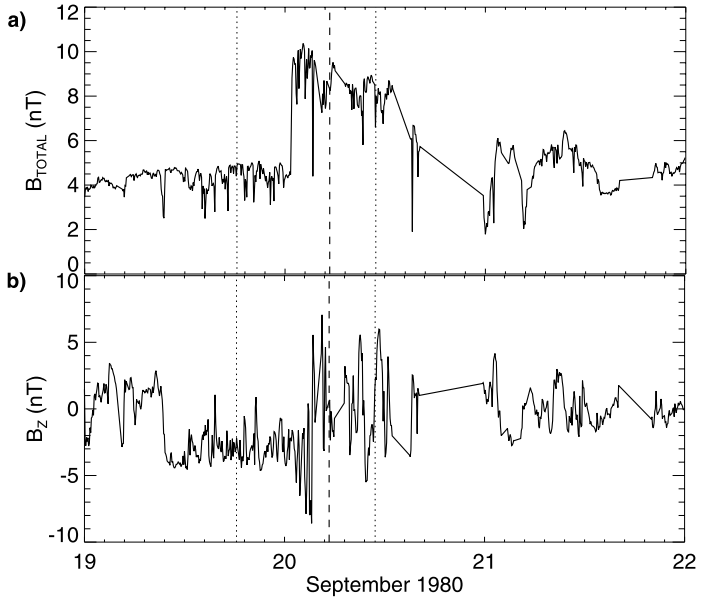

Figure 10 ISEE-3 Magnetometer data for the interval near the predicted arrival of the 17 September 1980 CME at Earth: (a) total field and (b) B_z. The vertical lines indicate the earliest, median and latest predicted arrival times.

Table 3 Summary of the TH fitting results for the 26 September 1980 CME. The columns are as for Table 1.

Run#	Launch Date	Speed $km\,s^{-1}$	Lon.	Lat.	Lon. Size	Lat. Size	Dist-ortion	Error	PCPA
~~0~~	~~19/09/80 02:26~~	~~188.1~~	~~-4.52~~	~~-0.65~~	~~36.72~~	~~43.22~~	~~1~~	~~4.93~~	~~98.22~~
1	20/09/80 12:13	208.63	−34.22	0	54.02	31.53	0.01	5.64	90
2	20/09/80 04:45	201.44	−9.12	6	36	23.99	0.09	5.61	56.45
3	22/09/80 00:45	258.92	−12	−5.98	50.51	40.98	0.07	5.86	116.76
4	21/09/80 03:33	230.29	−12	−5.97	44.98	36	0.14	5.71	116.69
5	20/09/80 04:29	201.21	−14.14	4.9	39.91	24	0.07	5.64	70.67
6	20/09/80 22:21	220.22	−12	10.65	43.6	24.01	0.04	5.66	47.88
7	22/09/80 08:14	271.15	−18	9.58	59.36	33.25	0.02	5.84	61.36
8	**21/09/80 10:33**	**239.62**	**−12.89**	**11.81**	**48.03**	**30**	**0.17**	**5.72**	**46.86**
9	22/09/80 02:55	261.99	−18	5.37	51.83	30.29	0.02	5.72	73.08
Avg	21/09/80 05:05	232.61	−15.82	4.04	47.58	30.45	0.07	5.71	75.53
Std	0.83	26.88	7.48	6.69	7.27	5.87	0.05	0.09	26.89
Med	21/09/80 03:33	230.29	−12.89	5.37	48.03	30.29	0.07	5.71	70.67
Min	20/09/80 04:29	201.21	−34.22	−5.98	36	23.99	0.01	5.61	46.86
Max	22/09/80 08:14	271.15	−9.12	11.81	59.36	40.98	0.17	5.86	116.76

Table 4 Summary of the predicted interactions of the 26 September CME with *in-situ* observing spacecraft.

Run#	Earth				PVO				*Helios-1*			
	Hit?	Date	Miss Dist (°)	Rcent (AU)	Hit?	Date	Miss Dist (°)	Rcent (AU)	Hit?	Date	Miss Dist (°)	Rcent (AU)
~~0~~	~~1~~	~~28/09/80 08:04~~	~~0~~	~~1~~	~~0~~	~~27/09/80 21:49~~	~~34.3~~	~~0.96~~	~~0~~	~~30/09/80 08:32~~	~~60.2~~	~~1.22~~
1	1	28/09/80 19:53	0	1	0	26/09/80 12:48	46.7	0.73	0	28/09/80 04:57	72.6	0.93
2	1	28/09/80 19:23	0	1	0	26/09/80 12:26	40.4	0.74	0	28/09/80 06:34	66.15	0.94
3	1	28/09/80 17:33	0	1	0	27/09/80 00:51	28.33	0.75	0	28/09/80 10:12	54.09	0.96
4	1	28/09/80 16:42	0	1	0	26/09/80 21:20	33.89	0.76	0	28/09/80 11:36	59.65	0.98
5	1	28/09/80 19:30	0	1	0	26/09/80 12:09	41.35	0.73	0	28/09/80 06:16	67.16	0.94
6	1	28/09/80 19:22	0	1	0	26/09/80 15:58	38.42	0.73	0	28/09/80 06:11	63.87	0.93
7	1	28/09/80 17:43	0	1	0	27/09/80 00:38	27.21	0.73	0	28/09/80 07:51	52.74	0.94
8	**1**	**28/09/80 17:23**	**0**	**1.01**	**0**	**27/09/80 00:59**	**34.24**	**0.78**	**0**	**28/09/80 14:19**	**59.58**	**0.99**
9	1	28/09/80 17:45	0	1	0	26/09/80 22:45	33.31	0.73	0	28/09/80 06:56	59.1	0.93
Avg		28/09/80 18:22	0	1		26/09/80 19:06	35.98	0.74		28/09/80 08:19	61.66	0.95
Std		0.05	0	0		0.24	6.32	0.02		0.13	6.39	0.02
Med		28/09/80 17:45	0	1		26/09/80 21:20	34.24	0.73		28/09/80 06:56	59.65	0.94
Min		28/09/80 16:42	0	1		26/09/80 12:09	27.21	0.73		28/09/80 04:57	52.74	0.93
Max		28/09/80 19:53	0	1.01		27/09/80 00:59	46.7	0.78		28/09/80 14:19	72.6	0.99

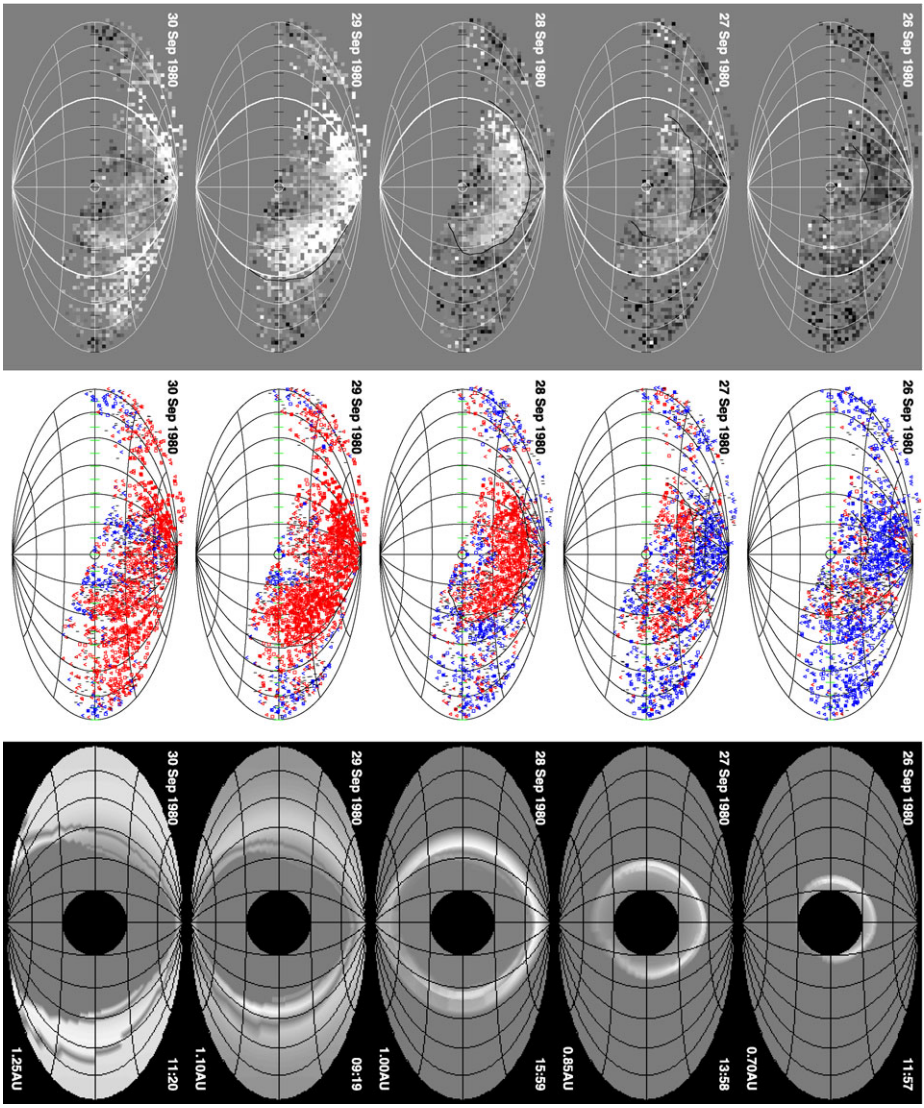

Figure 11 g-maps for the 26 September 1980 event in the same format as Figure 4, the simulations are from Run #8.

not seen beyond 26 September. A three-dimensional view and its relationship to Earth and the other available observing platforms is illustrated in Figure 13.

Tappin (1984) did not perform a detailed fit for this event, but concluded that it was large and rather slow, with an estimated speed of about 400 km s^{-1}. As with the previous event this is significantly faster than the speeds that we find.

As with the previous event we were able to perform a stage 2 fitting to this CME, the results are shown in Figure 14. Again we see a marked deceleration from an already slow speed of 301 km s^{-1} between 26 and 27 September to 215 km s^{-1}.

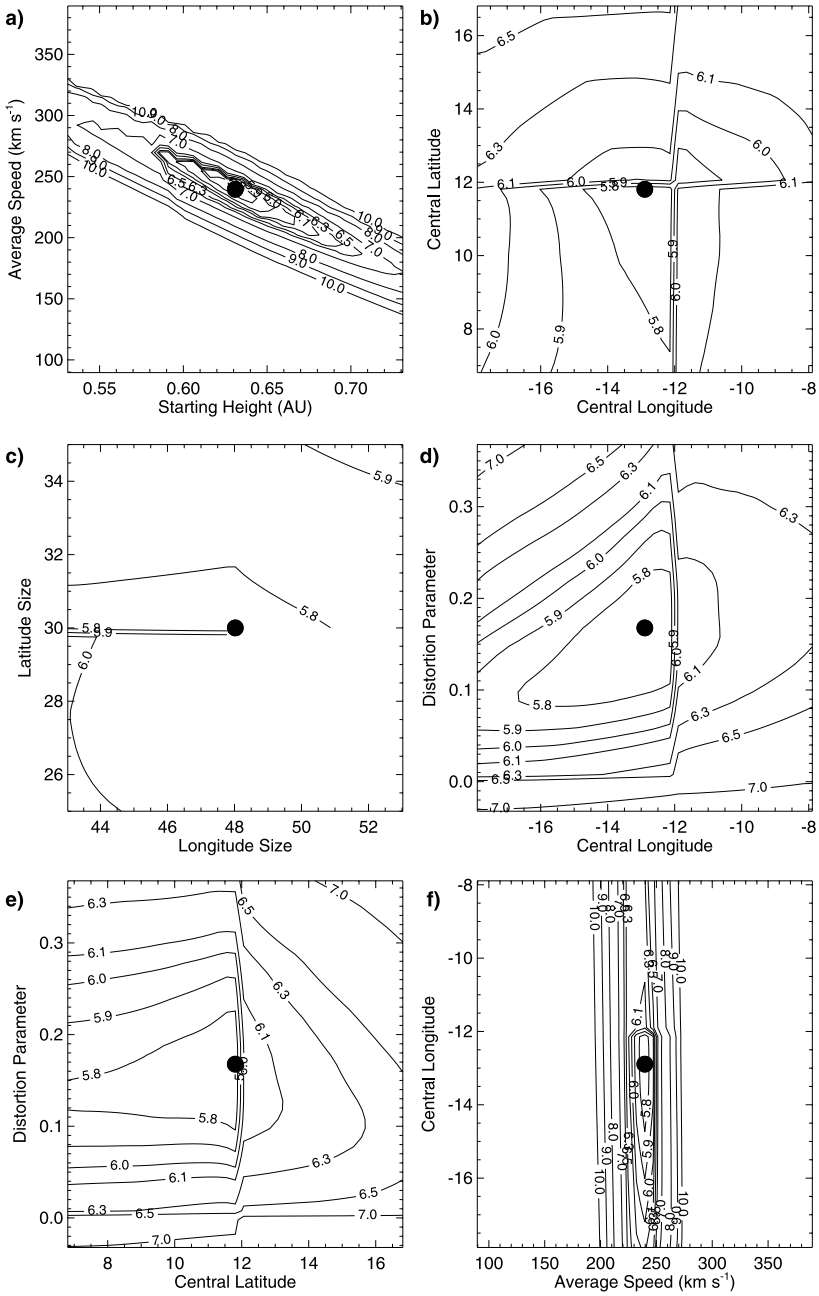

Figure 12 Selected error surfaces for the fit to the 26 September 1980 CME, the format is identical to that of Figure 5, in this case the time of the starting height is 00:00 UT on 26 September.

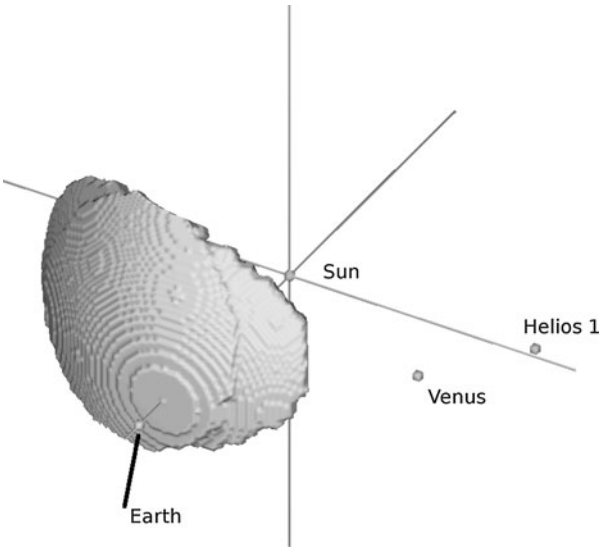

Figure 13 3-D view of the fitted leading surface of the 26 September 1980 CME from 35N30W when the leading edge was at 0.9 AU (22:38 UT on 27 September), as in Figure 6 the locations of the Sun, Earth, Venus (PVO) and *Helios-1* are shown.

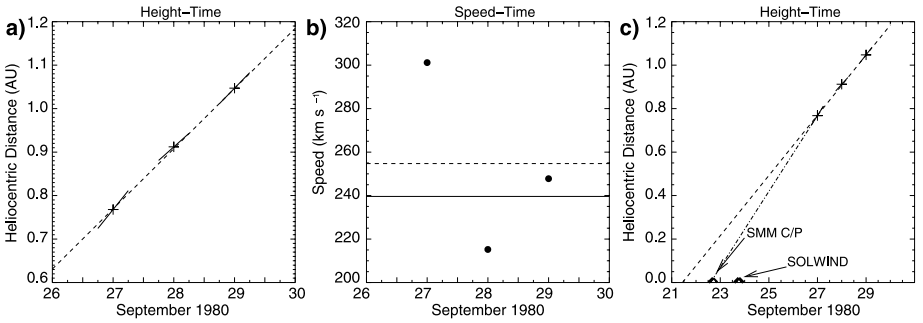

Figure 14 Stage 2 fitting results for the 26 September 1980 CME. The layout of the panels is as for Figure 7; however, in panel (c) the times of the SMM C/P and SOLWIND CMEs are added.

The launch timing and longitude for this event are shown in relation to the GOES flares in Figure 8. In this case there was a line of N-hemisphere flares following the event that projects back to near the centre of the CME, and so is probably related to the same area of the Sun. There was a M1.1 flare at 07:42 UT on 22 September identified at N20W03, and an M2.5 at 16:08 on 23 September, with no optical identification. Both of these were associated with Type II bursts *Solar Geophysical Data* (1980, 1981). There were no significant events seen in the HXIS dataset during the probable launch interval.

The SMM C/P catalogue lists an apparently very slow ($< 20\,\mathrm{km\,s^{-1}}$) eruption at the very end of their data from 17:00 UT on 22 September to 02:35 UT on 23 September. The SOLWIND coronagraph does not have images available for 20 – 22 September, but reports three events on 23 September (N.R. Sheeley Jr., private communication). These data suggest the ejection of material in the SE around 17:30 UT on 23 September. These CMEs are compared with the fitted height – time relation for the IPS disturbance in Figure 14(c). As the speeds we compute from the IPS observations are extremely slow, it is possible

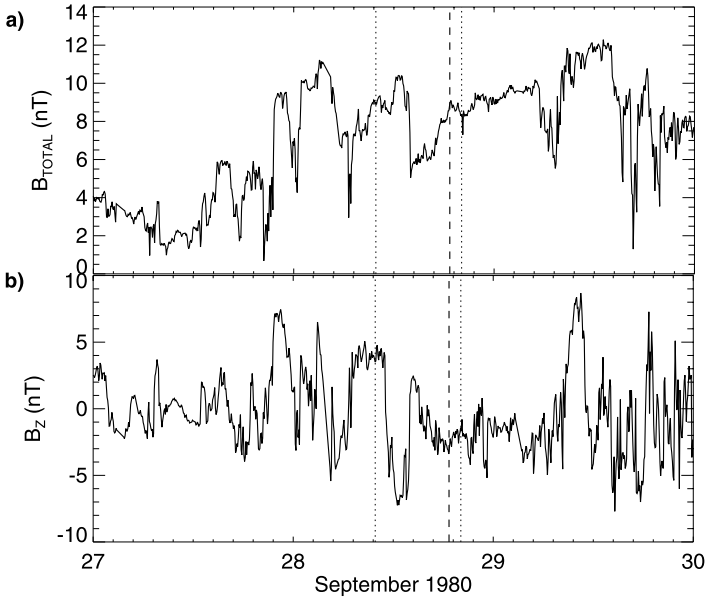

Figure 15 ISEE-3 Magnetic field data for the interval around the arrival of the 26 September 1980 CME at Earth. (a) Total field, (b) Z-component. The dashed vertical line indicates the median time, and the dotted lines indicate the earliest and latest times.

that we have somewhat underestimated the speed or that the CME decelerated in transit, in which case either of these events is consistent with being the source of the disturbance. We think it probable that these are connected with the two Type II bursts and that one is the event we observe in IPS, but we cannot be sure which. The SMM C/P event appears the more likely source of the IPS event as the SOLWIND event would require an average speed of about 440 $\mathrm{km\,s^{-1}}$ to the start of the IPS observations, which is twice the speed in the IPS observations, the SMM C/P event on the other hand would need an average speed of 315 $\mathrm{km\,s^{-1}}$, only about 50% faster than the we fitted and very close to the speed from the stage 2 fit to 26 and 27 September.

The near-Earth observations for this disturbance (Figures 9 and 15) are somewhat confusing. There is no clear signature of an event hitting the Earth, despite the IPS observations leaving very little doubt that a large, slow disturbance arrived. The arrival time is too-well constrained to allow the density and field rise late on 27 September (Day 271) to correspond to the leading edge; however the rise is relatively slow and so we presume that the edge we see in the *g*-maps lies some way behind the rise seen by the *in-situ* measurements.

According to the fitting, this disturbance should not reach all the way to *Pioneer Venus Orbiter* (PVO) at 0.72 AU, 66.5°W or *Helios-1* at 0.92 AU, 92.4°W. However the PVO data (Figures 16 and 17) do show a high-speed feature at about the time that the structure came closest to PVO and there is also a broadening of the Venus-related peak at the same time which is probably indicative of a solar wind disturbance. However the fact that the density is enhanced several days before this is more characteristic of a high-speed stream than of a CME. The speed and density are both rising at *Helios-1* at the time of interest and there is a peak in density and speed within the window of arrival times, however any feature in the magnetic field is very weak. Tappin (1984) thought it possible that these features were

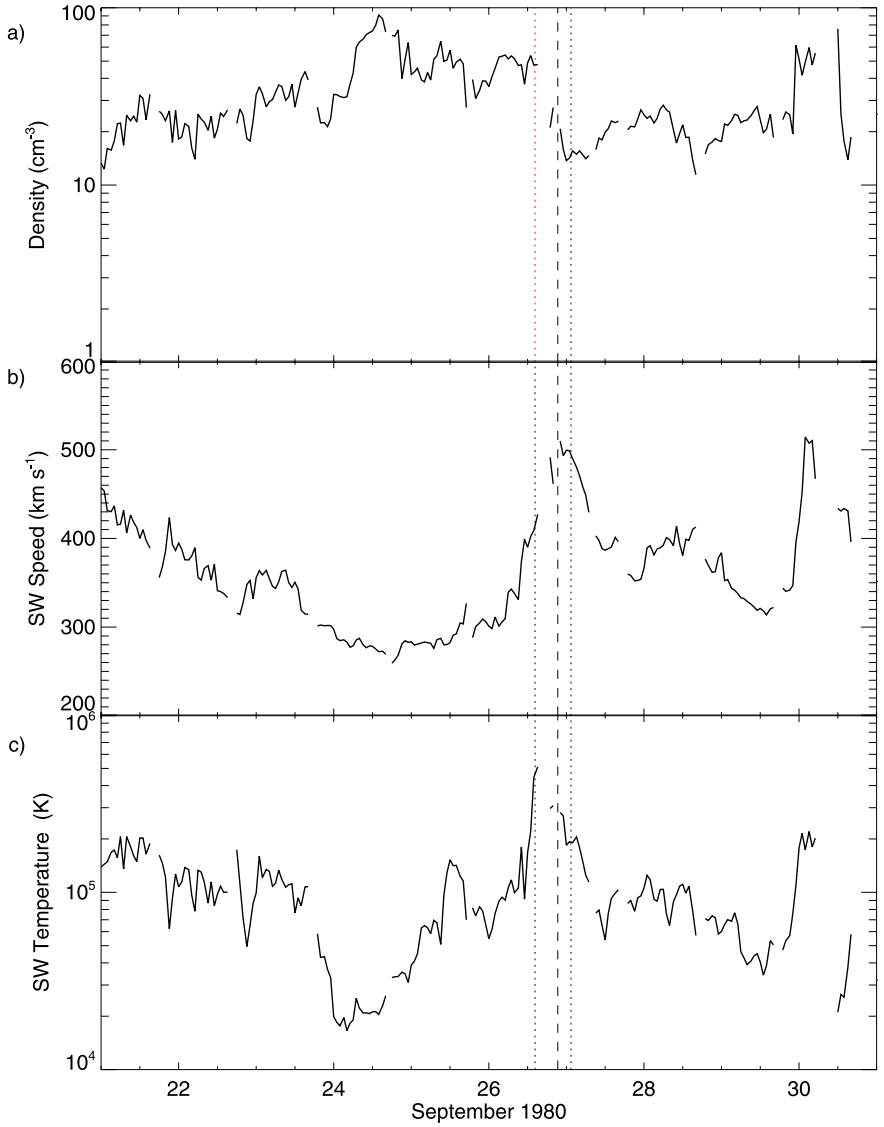

Figure 16 PVO plasma data for the time around the closest approach of the 26 September CME. (a) Density, (b) solar wind speed and (c) proton temperature. The time of closest approach is indicated by the vertical lines.

a signature of the same event, however the original estimate was that the disturbance was directed slightly West, while our fits suggest it was slightly East. This difference is easily accounted for by the fact that in the original study, the time-smearing through the course of each map was accounted for only qualitatively. If it were the same event then it would require an exceptionally large extent in longitude, certainly over 120° and probably nearer to 180°. For this reason we consider it more likely that the near-coincidence in time of the features seen at Earth, PVO and at *Helios-1* is just a coincidence.

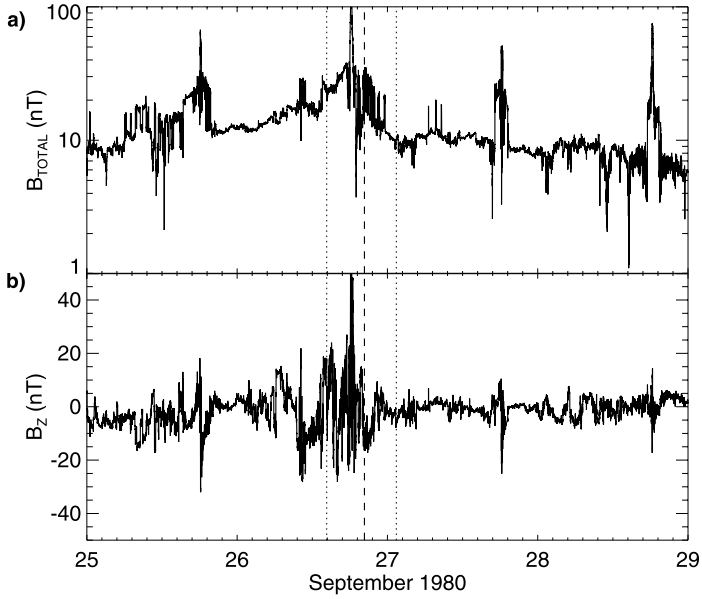

Figure 17 PVO Magnetometer data for the interval around the closest approach of the 26 September 1980 CME. (a) Total field and (b) Z-component. Note that the peaks in field magnitude at around 17:00 UT each day are produced when the spacecraft was occulted from the solar wind flow by Venus (C.T. Russell, private communication). The vertical lines indicate the earliest, latest and median values of the time of closest approach.

6. Discussion and Conclusions

In the foregoing sections we have described the modification of the TH model to allow it to be used on IPS data. We have then applied it to two major CMEs that were observed in September of 1980. The question we must now address is whether the TH approach to fitting CME structures is as applicable to IPS observations as it is to white-light observations.

Obviously the biggest difference in the observations, from the point of view of the user, is the much lower cadence of the IPS observations. Whereas SMEI generates a sky map every 102 minutes and the STEREO HI-2s generate an image every two hours, the 3.6 ha Array could only generate one map per day. The events we chose for this study were specifically chosen for having three or more days on which a leading edge could be distinguished. We find that three maps as compared with the 10 – 20 from a white-light imager do not cause inconsistent convergences. This is because although there are fewer points they are still spread over a sufficiently long interval, or more importantly over a large range of heliocentric distances. Since the time of observation at a given point on the map can be computed, the "focal plane shutter" distortion of the CME image which is much greater than for a white-light imager can be quantitatively accounted for by the TH model. Although the northerly location of the telescope limits us to about 180° of position-angle coverage, this is in practice comparable with or greater than is typically obtained with the current generation of white-light imagers.

We have found that in these two cases, the TH model converged as well as it typically does for white-light images. We think it very probable that for faster events, which were only seen on two days, the fitting parameters would be poorly constrained. From a practical space

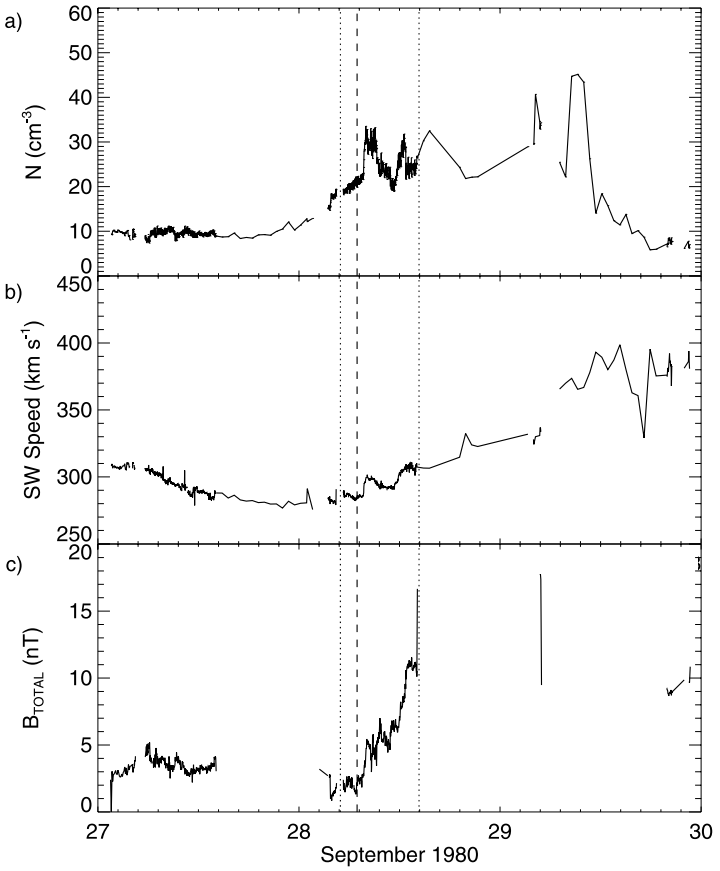

Figure 18 *Helios-1* plasma and field data for the interval around the closest approach of the 26 September 1980 CME. (a) Density, (b) solar wind speed and (c) total field. The vertical lines indicate the range and median fitted closest approach times.

weather forecasting perspective, these problems could be overcome by the use of multi-beam instruments at several sites widely spaced in longitude (as is done for the flare patrol optical telescopes). For example if there were four telescopes distributed in longitude and latitude and each capable of looking $\pm 30°$ from the meridian, then the low-latitude cadence could be around two to three hours with some eight-hour gaps at high latitudes.

One significant discrepancy from the "eyeball" fitting previously performed (Tappin, 1984, 1987) is that the speeds we find are significantly slower. When we look at the stage 2 fitting results we find that in both cases the first day of observations leads to a much higher speed, comparable with the older fitting. This leads us to speculate that the decelerations may not be a real effect, but a result of a problem with the assumptions about the scattering properties of the medium. The older fitting was done by comparing entire maps of the disturbance with maps of the models including times after the CME had passed Earth while the present work only compares leading edges. Therefore anything which could change the apparent location of the leading edge when the CME was near to Earth, but left the overall structures further away unchanged could produce this discrepancy. The obvious candidate for such an effect would be the Fresnel zone, the region near to the observer which does not

contribute significantly to the scintillation index. The size of this zone is determined by the scale size of the medium a in Equation (3), and if the scale size were larger than the value we have adopted, then the Fresnel zone would also be larger. When we look at the determination of the scale size by Readhead, Kemp, and Hewish (1978), in particular their Figure 7, it appears that a scale size of 300 km at 1 AU would be possible. However if we adopt that value, the apparent leading edge of a large halo CME is moved by only a little over 1° when it is close to 1 AU, which is insufficient to account for a deceleration from 300 $\mathrm{km\,s^{-1}}$ to little over 200 $\mathrm{km\,s^{-1}}$. Therefore at present this remains a puzzle that requires further study. Unfortunately the manner in which the data for these observations were collected precludes their use for a similar analysis to that of Readhead, Kemp, and Hewish (1978).

Although the supporting data are somewhat sparse, we do not find any major discrepancies between our inferences and those from other observations giving us confidence that the TH model has done a good job of reconstructing the large-scale parameters of the CMEs.

The temporal coincidences of the probably-unrelated features seen at Earth, PVO and *Helios-1* at the time of the 26 September CME, shows why it is important to have an imaging capability whether in white light or in IPS, especially at times of high solar activity.

In conclusion we find that IPS could provide a capable alternative to white light as a means of imaging disturbances in the heliosphere, although the data cadence means that to be a useful forecasting tool multiple telescopes would be needed. We have also shown that the TH model is as able to reconstruct CMEs from IPS g-maps as it is from white-light images.

Acknowledgements We wish to thank the following persons and institutions who have made data available: H. Rosenbauer, R. Schwenn, Max Planck Institut, Lindau (*Helios* solar wind data); J.T. Gosling, MIT, Los Alamos National Lab. (ISEE-3 Plasma); E.J. Smith, UCLA (ISEE-3 Magnetometer); UC Berkeley, (ISEE-3, IMP8 & *Helios* data hosting); C.T. Russell, UCLA (PVO Magnetometer); P.R. Gazis, NASA Ames (PVO Plasma); HAO (SMM C/P); N.R. Sheeley Jr., NRL (SOLWIND). The LASCO CME catalogue is generated and maintained at the CDAW Data Center by NASA and The Catholic University of America in cooperation with the Naval Research Laboratory. SOHO is a project of international cooperation between ESA and NASA. The National Solar Observatory is operated by AURA Inc., under a cooperative agreement with the National Science Foundation, partial support for NSO is provided by the USAF under a memorandum of agreement. T.A.H.'s work was supported by SwRI internal project 15-R8092. The construction and operation of the 3.6 ha Array was funded by the UK Science Research Council.

References

Baker, D.N., Balstad, R., Bodeau, J.M., Cameron, E., Fennell, J.F., Fisher, G.M., Forbes, K.F., Kintner, P.L., Leffler, L.G., Lewis, W.S., Reagan, J.B., Small, A.A. III, Stansell, T.A., Strachan, L. Jr.: 2009, *Severe Space Weather Events: Understanding Societal and Economic Impacts*, The National Academies Press, Washington.

Brueckner, G.E., Howard, R.A., Koomen, M.J., Korendyke, C.M., Michels, D.J., Moses, J.D., Socker, D.G., Dere, K.P., Lamy, P.L., Llebaria, A., Bout, M.V., Schwenn, R., Simnett, G.M., Bedford, D.K., Eyles, C.J.: 1995, *Solar Phys.* **162**, 357.

Budden, K.G., Uscinski, B.J.: 1970, *Proc. Roy. Soc. Lond. A* **316**, 315.

Budden, K.G., Uscinski, B.J.: 1971, *Proc. Roy. Soc. Lond. A* **321**, 15.

Budden, K.G., Uscinski, B.J.: 1972, *Proc. Roy. Soc. Lond. A* **330**, 65.

Burkepile, J.T., St. Cyr, O.C.: 1993, NCAR Technical Note TN-369+STR, http://smm.hao.ucar.edu/smmcp_catalog.html.

Couzens, D.A., King, J.H.: 1986, Interplanetary Medium Data Book – Supplement 3a. NASA/NSSDC.

Dungey, J.W.: 1963, *Planet. Space Sci.* **10**, 233.

Emslie, A.G., Kucharek, H., Dennis, B.R., Gopalswamy, N., Holman, G.D., Share, G.H., Vourlidas, A., Forbes, T.G., Gallagher, P.T., Mason, G.M., Metcalf, T.R., Mewaldt, R.A., Murphy, R.J., Schwartz, R.A., Zurbuchen, T.H.: 2004, *J. Geophys. Res.* **109**, A10104.

Eyles, C.J., Simnett, G.M., Cooke, M.P., Jackson, B.V., Buffington, A., Hick, P.P., Waltham, N.R., King, J.M., Anderson, P.A., Holladay, P.E.: 2003, *Solar Phys.* **217**, 319.
Eyles, C.J., Harrison, R.A., Davis, C.J., Waltham, N.R., Shaughnessy, B.M., Mapson-Menard, H.C.A., Bewsher, D., Crothers, S.R., Davies, J.A., Simnett, G.M., Howard, R.A., Moses, J.D., Newmark, J.S., Socker, D.G., Halain, J.-P., Defise, J.-M., Mazy, E., Rochus, P.: 2009, *Solar Phys.* **254**, 387.
Gapper, G.R., Hewish, A., Purvis, A., Duffett-Smith, P.J.: 1982, *Nature* **296**, 633.
Gosling, J.T., Ashbridge, J.R., Bame, S.J., Hundhausen, A.J., Strong, I.B.: 1968, *Astron. J.* **73**, 61.
Gosling, J.T., Hildner, E., MacQueen, R.M., Munro, R.H., Poland, A.I., Ross, C.L.: 1974, *J. Geophys. Res.* **79**, 4581.
Hewish, A.: 1993, In: Tatarskii, Ishimaru, Zavorotny (eds.) *Wave Propagation in Random Media (Scintillation)*, SPIE/IOP, Bellingham, 261.
Hewish, A., Scott, P.F., Wills, D.: 1964, *Nature* **203**, 1214.
Houminer, Z.: 1971, *Nat. Phys. Sci.* **231**, 165.
Houminer, Z., Hewish, A.: 1972, *Planet. Space Sci.* **21**, 1703.
Howard, R.A., Moses, J.D., Vourlidas, A., Newmark, J.S., Socker, D.G., Plunkett, S.P., Korendyke, C.M., Cook, J.W., Hurley, A., Davila, J.M., Thompson, W.T., St. Cyr, O.C., Mentzell, E., Mehalick, K., Lemen, J.R., Wuelser, J.P., Duncan, D.W., Tarbell, T.D., Wolfson, C.J., Moore, A., Harrison, R.A., Waltham, N.R., Lang, J., Davis, C.J., Eyles, C.J., Mapson-Menard, H., Simnett, G.M., Halain, J.P., Defise, J.M., Mazy, E., Rochus, P., Mercier, R., Ravet, M.F., Delmotte, F., Auchere, F., Delaboudiniere, J.P., Bothmer, V., Deutsch, W., Wang, D., Rich, N., Cooper, S., Stephens, V., Maahs, G., Baugh, R., McMullin, D., Carter, T.: 2008, *Space Sci. Rev.* **136**, 67.
Howard, T.A., Tappin, S.J.: 2009a, *Space Sci. Rev.* **147**, 31.
Howard, T.A., Tappin, S.J.: 2009b, *Space Sci. Rev.* **147**, 89.
Howard, T.A., Tappin, S.J.: 2010, *Space Weather*, in press. doi:10.1029/2009SW000531.
Hundhausen, A.J., Burkepile, J.T., St. Cyr, O.C.: 1994, *J. Geophys. Res.* **99**, 6543.
Kemp, M.C.: 1979, PhD Thesis, University of Cambridge.
Low, B.C.: 1996, *Solar Phys.* **167**, 217.
Ogilvie, K.W., von Rosenvinge, T., Durney, A.C.: 1977, *Science* **198**, 131.
Purvis, A., Tappin, S.J., Rees, W.G., Hewish, A., Duffett-Smith, P.J.: 1987, *Mon. Not. Roy. Astron. Soc.* **229**, 589.
Readhead, A.C.S., Kemp, M.C., Hewish, A.: 1978, *Mon. Not. Roy. Astron. Soc.* **185**, 207.
St. Cyr, O.C., Hundhausen, A.J., Burkepile, J.T.: 1992, In: *ESA, Proceedings of the First SOHO Workshop: Coronal Streamers, Coronal Loops, and Coronal and Solar Wind Composition*, 125.
St. Cyr, O.C., Howard, R.A., Sheeley, N.R., Plunkett, S.P., Michels, D.J., Paswaters, S.E., Koomen, M.J., Simnett, G.M., Thompson, B.J., Gurman, J.B., Schwenn, R., Webb, D.F., Hildner, E., Lamy, P.L.: 2000, *J. Geophys. Res.* **105**, 18169.
Scheuer, P.A.G.: 1957, *Proc. Camb. Philos. Soc.* **53**, 764.
Shishov, V.I.: 1993, In: Tatarskii, Ishimaru, Zavorotny (eds.) *Wave Propagation in Random Media (Scintillation)*, SPIE/IOP, Bellingham, 272.
Solar Geophysical Data: 1980, 1981, Prompt and Comprehensive reports; NOAA NGDC.
Sonett, C.P., Colburn, D.S., Davis, L., Smith, E.J., Coleman, P.J.: 1964, *Phys. Rev. Lett.* **13**, 153.
Stone, E.C., Frandsen, A.M., Mewaldt, R.A., Christian, E.R., Margolies, D., Ormes, J.F., Snow, F.: 1998, *Space Sci. Rev.* **86**, 1.
Tappin, S.J.: 1984, PhD Thesis, University of Cambridge.
Tappin, S.J.: 1986, *Planet. Space Sci.* **34**, 93.
Tappin, S.J.: 1987, *Planet. Space Sci.* **35**, 271.
Tappin, S.J., Howard, T.A.: 2009, *Space Sci. Rev.* **147**, 55.
Tappin, S.J., Buffington, A., Cooke, M.P., Eyles, C.J., Hick, P.P., Holladay, P.E., Jackson, B.V., Johnston, J.C., Kuchar, T., Mizuno, D., Mozer, J.B., Price, S., Radick, R.R., Simnett, G.M., Sinclair, D., Waltham, N.R., Webb, D.F.: 2004, *Geophys. Res. Lett.* **31**, L02802.
Tatarskii, V.I.: 1993, In: Tatarskii, Ishimaru, Zavorotny (eds.) *Wave Propagation in Random Media (Scintillation)*, SPIE/IOP, Bellingham, 2.
Tousey, R.: 1973, In: Rycroft, M.J., Runcorn, S.K. (eds.) *Proceedings of Open Meetings of Working Groups of the 15th Plenary Meeting of the Committee on Space Research (COSPAR)*, Madrid, Spain, May 10 – 24, 1972. Akademie Verlag, Berlin and Pergamon, Oxford, 713.
Zhao, X.P., Plunkett, S.P., Liu, W.: 2002, *J. Geophys. Res.* **107**, 1223.